Acta Materialia 186 (2020) 215–222

Contents lists available at ScienceDirect

Acta Materialia

journal homepage: www.elsevier.com/locate/actamat

Full length article

Mechanical properties of metallic lithium: from nano to bulk scales

Cole D. Fincher[a], Daniela Ojeda[b], Yuwei Zhang[a], George M. Pharr[c], Matt Pharr[a,*]

[a] Department of Mechanical Engineering, Texas A&M University, College Station, Texas, 77840 United States
[b] Department of Mechanical and Aerospace Engineering, University of Central Florida, Orlando, Florida, 32816, United States
[c] Department of Materials Science and Engineering, Texas A&M University, College Station, Texas 77840, United States

ARTICLE INFO

Article history:
Received 11 September 2019
Revised 18 December 2019
Accepted 19 December 2019
Available online 23 December 2019

Keywords:
Lithium metal
Li-ion batteries
Mechanical properties
Dendrite formation
Plasticity

ABSTRACT

Despite renewed interest in lithium metal anodes, unstable electrodeposition of Li during operation has obstructed progress in practical battery applications. While deformation mechanics likely play a key role in Li's mechanical stability as an anode material, reports of Li's mechanical properties vary widely, perhaps due to variations in testing procedures. Through bulk tensile testing and nanoindentation, we provide a comprehensive assessment of the strain-rate and length-scale dependent mechanical properties of Li in its most commonly used form: high purity commercial foil. We find that bulk Li exhibits a yield strength between 0.57 and 1.26 MPa for strain rates from 5E-4 s^{-1} to 5E-1 s^{-1}. For indentation tests with target $\dot{P}/P = 0.05\ s^{-1}$, the hardness decreases precipitously from nearly 43 MPa to 7.5 MPa as the indentation depth increases from 250 nm to 10 μm. The plastic properties measured from bulk and nanoindentation testing exhibit strong strain-rate dependencies, with stress exponents of $n = 6.55$ and 6.9, respectively. We implement finite element analysis to relate the indentation depth to length scales of relevance in battery applications. Overall, the results presented herein may provide important guidance in designing Li anode architectures and charging conditions to mitigate unstable growth of Li during electrochemical cycling.

1. Introduction

Realization of pure lithium anodes would enable transformative rechargeable battery systems with significantly greater theoretical energy capacities, such as Li-S (2.6 kWh/kg) and Li-Air (3.5 kWh/kg), as compared to current commercial materials such as C-$LiCoO_2$ (0.4 kWh/kg) [1]. Indeed, Li metal is known as the "Holy Grail" of anode materials, as it has the highest theoretical capacity, lowest density, and most negative electrochemical potential of the candidate materials [2]. While a few commercial interests first pursued Li metal batteries nearly 50 years ago, safety concerns preempted its widespread adoption. Early studies found that Li forms dendrites during repeated cycling, leading to short circuits, thermal runaway, and explosion hazards [2]. However, the increasing need for high-energy density power sources has led to a renaissance in Li metal research. Likewise, increased study of both liquid and solid-state electrolytes (SSEs) have paved the way towards safer batteries. However, maintaining reversible Li deposition during cycling has still proven problematic in many battery systems [3-6].

A few studies have shown that the deformation mechanics of the component materials play a key role in the formation/suppression of Li dendrites and the corresponding interfacial stability [7,8]. The seminal work of Newman and Monroe suggested that the pressure applied to the surface of the anode via the separator directly affects the propensity for dendrite formation [9]. Recently, the results of Jana and Garcia indicate that dendrite morphology and growth are a direct product of the competition between the rate of Li deposition and the rate of Li's plastic deformation under pressure [10]. Implicitly, Jana and Garcia's findings may suggest that the morphology of lithium possesses a strong dependency on charging rate and feature size. Meanwhile, experimental studies by Gireaud et al. [11], Wilkinson et al. [12], and Hirai et al. [13] attest to the effects of pressure on the Li deposition morphology, and studies by Dollé et al. [14], Brissot et al. [15], and others demonstrate that a strong rate-dependency of Li deposition morphology exists across multiple length scales [16]. Beyond the growth of dendrites in liquid electrolyte systems, multiple studies outline the importance of deformation mechanics in maintaining stable interfacial contact between the SSE and the anode in all-solid-state batteries (ASSB's) [2–4,6,17–20]. For instance, Li et al. observed improved battery performance with increased interfacial contact under mechanical loading for an ASSB [5]. Taken together,

* Corresponding author.
E-mail address: m-pharr@tamu.edu (M. Pharr).

https://doi.org/10.1016/j.actamat.2019.12.036
1359-6454/

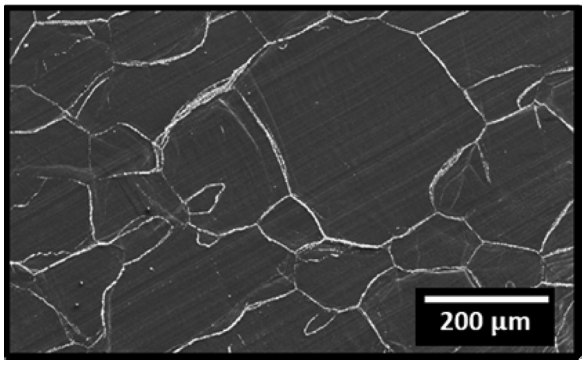

Fig. 1. A scanning electron micrograph of Li foil prior to surface preparation. The grain size is near 110 ± 20 µm (average ± standard deviation) using the linear intercept technique.

these studies suggest the potential to harness mechanics for realizing more stable Li electrodeposition.

While a few recent studies have measured some of the mechanical properties of Li, the community still lacks a holistic multi-length and time scale portrait. Three individual studies of lithium metal under compression at the nano-[21], micro-[22], and bulk [23] scales suggest that the yield strength of Li varies by significantly more than an order of magnitude. Additionally, studies of lithium metal in tension by Tariq et al. [24], followed very recently by Masias et al. [25] and LePage et al. [26], indicate highly ductile and strain-rate dependent plasticity in bulk lithium. However, directly comparing these results proves problematic, given the studies' various methods of sample preparation and loading conditions (e.g., geometries and rates). For instance, recent work by Campbell et al. suggests that cold-working of lithium metal can alter its hardness by nearly an order of magnitude [27]. In addition, relating mechanical measurements for Li metal to the mechanical properties of Li electrodeposits requires careful consideration of the plastic volumes deforming during mechanical testing, which are typically much smaller in nanoindentation than in bulk tensile testing. Given these potentially confounding factors, reliably representing the deformation mechanics of Li dendrites requires a comprehensive study of lithium metal as commercially prepared for practical battery applications and over the relevant length and time scales.

To this end, this paper provides a mechanical study of the most commonly used form of Li metal in the battery community: high-purity Li metal foil. Through a combination of bulk tensile testing, nanoindentation, and finite element analysis, we systematically characterize the mechanical properties of Li metal across length scales, nano to bulk, and time scales, by varying the loading rates over a significant range. We also detail the implications of these measurements in terms of the performance of Li metal anodes.

2. Methods

2.1. Li sample preparation for nanoindentation

As-received lithium foil, as seen in Fig. 1, possesses significant surface roughness and occasionally chemical contamination. Thus, the indentation samples required careful preparation prior to testing. All sample preparation and indentation occurred within an argon-filled glovebox with less than 0.1 ppm O_2 and H_2O. The lithium foil (Sigma Aldrich, 99.9% purity on trace metal basis) was first sectioned into an 8 mm by 8 mm square and adhered to a nanoindentation mount at 70°C using Crystal Bond 555 adhesive. The surface of the foil was prepared by shaving it with a razor blade to reveal fresh lithium with minimal surface contamination. The sample and indentation mount was placed between two well-oiled borosilicate glass plates (1/4-inch-thick, lubricated with Sonneborn PD-28 highly refined white mineral oil), and the plates were placed inside a hydraulic crimper and pressed until the Li was flat. The sample and indentation mount were immediately removed and mounted on the nanoindenter, also located within the glovebox. An optical micrograph of an indentation made in this way is shown in Fig. S1. By conducting experiments on an as fabricated sample before and after a 24 hour anneal at 0.8 * T_m, we assessed potential of surface damage due to sample preparation. Full details can be found in the supplementary information section titled "Assessing the possibility of surface damage during sample preparation." In summary, however, we find minimal changes in hardness after annealing at 0.8 * T_m, which implies that the sample preparation is unlikely to affect the hardness measurements presented in this study.

2.2. Nanoindentation methods

Nanoindentation measurements of hardness, H, and elastic modulus, E, were made using a Nanomechanics Nanoflip indentation system operated in the glove box. All measurements were performed with a Berkovich triangular pyramid indenter using the continuous stiffness measurement technique (CSM) [28,29].

Continuous stiffness measurements of mechanical properties require precise knowledge of the indenter area function, which is normally determined in tests of a fused silica calibration standard [28,29]. However, in this study, an area function was required to much larger depths than can be achieved in fused silica. As such, the fused silica area function was supplemented by calibration measurements from polycarbonate (Makrolon®, 0.08 inch thickness, ASTM D3935 class 1 polycarbonate sheet) in a manner similar to that described by Ginder and Pharr [30]. This area function was calibrated over the range of 250 nm to 10 μm; thus, E and H measurements outside of this range are discarded.

Lithium has an extremely high modulus-to-hardness ratio E/H (in the range 500-1000), and consequently, very little elastic recovery occurs during unloading; in fact, the depth recovery is less than 1% of the total penetration depth, h. Using this observation, the total depth of penetration can conveniently be used as a good measure of the contact depth, h_c, (therefore rendering the sink-in correction to contact depth unnecessary), provided that one important correction is made. Specifically, lithium is a material that exhibits pile-up during indentation, which is not properly accounted for in standard nanoindentation data analysis procedures. To include pile-up effects here, several large indentations were optically imaged under oil and measured to determine the contact area. Based on the known area function, these measurements indicated that due to pile-up, the contact depth is 11% greater than the measured indenter penetration depth, that is, $h_c/h = 1.11$. Thus, the depth used in evaluating the contact area A_c was taken as 1.11 times the measured indenter penetration depth. The hardness then followed from $H = P/A_c$, where P is the instantaneous indentation load. We should note that the degree of pile up depends significantly upon the E/H ratio of a material, and thus accuracy of the pile-up assumption (that $h_c/h = 1.11$) may vary with depth for a material with depth-dependent hardness [28].

An important factor in accurately measuring the modulus of lithium by nanoindentation CSM methods is what has recently been identified Merle et al. as "plasticity error" [26]. This systematic error originates from a breakdown in the assumption that deformation during the small force oscillation used to make CSM measurements is entirely elastic, that is, there is no plastic deformation induced by the oscillation. Plasticity error becomes significant in materials with higher E/H ratios, like lithium. Fortunately, it has also been found that if the phase shift between

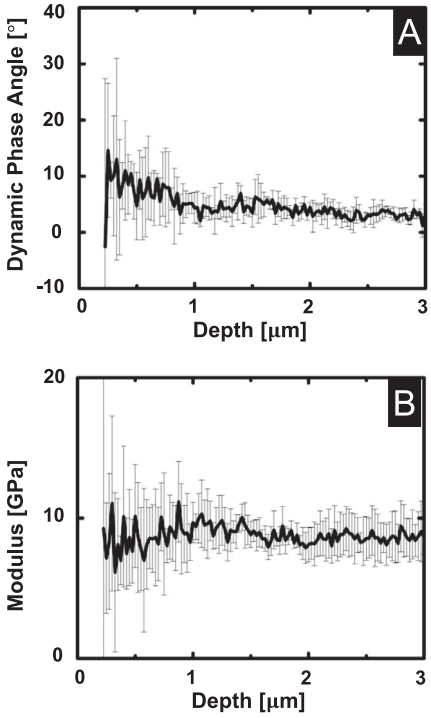

Fig. 2. Nanoindentation tests, with the curves representing the average of five indents and the error bar representing the standard deviation of the set of indents. Displayed tests were conducted with a constant $\dot{P} = 12.5\frac{\mu N}{s}$ to a depth of 3 μm. (A) the dynamic phase angle suggesting negligible plasticity error, (B) the elastic modulus. Individual tests can be seen in Figure S2.

the force and displacement oscillations as measured by the lock-in amplifier used to make the CSM measurement is less than 10°, then plasticity error is negligible [26,27]. Indeed, the measurements in Fig. 2 meet this 10° criteria, allowing for the use of continuous stiffness to collect the contact stiffness and ultimately measure the elastic modulus.

It is notable that the measurements in Fig. 2B based on the Oliver-Pharr approach (using the measured dynamic stiffness and depths between 0.25 and 3 μm) yield an elastic modulus of 9.43 ± 0.5 GPa that is independent of depth. Since this modulus is consistent with previous studies, the data suggest that the measurements at the depths reported here are not influenced in any significant way by an oxide/nitride/hydroxide or other contaminant layer on the surface.

2.3. Tensile testing

A custom-built tensile tester was configured within the glovebox for the purpose of performing tests in a controlled environment most suitable for the air-sensitive lithium without having to transfer the specimens. The apparatus (seen in Fig. S3) consisted of a LC703-200 load cell (Omega Engineering) in conjunction with an INF-USB2 model data acquisition system (Interface Inc.), and a ClearPath-MCPV model integrated servo motor system (Teknic) assembled onto an FGS-250W test stand (SHIMPO). The load cell calibration was validated against an Instron 5943 benchtop tensile tester with a 1 kN load cell (Fig. S4). To further ensure the system's accuracy, standard high density polyethylene (HDPE) tensile specimens were tested both with the in-glovebox tensile tester and with the benchtop tensile tester (Instron 5943) at strain rates of 5E-1 s^{-1} and 5E-4 s^{-1} (Fig. S5), with 100 Hz and 10 Hz acquisition rates, respectively. For the lithium data, we also implemented a toe compensation to mitigate the effects of system slack [31]. Additionally, a machine compliance determination (effects of which are seen in Fig. S6), was conducted in accordance with the procedure outlined by Kalidindi, Abusafieh and El-Danaf [32], taking the elastic modulus of lithium as 9.4 GPa as determined in this study (from Fig. 2B).

Lithium metal ribbon (Sigma Aldrich, 99.9% purity on trace metal basis), 45 mm wide and 0.75 mm thick, was stored in an argon-filled glovebox with less than 0.1 ppm O_2 and H_2O. A dogbone-shaped die (gauge width of 10 mm and length of 55 mm, 5 mm fillet radius, and total length of 105 mm) was used to stamp out the test specimens from the as-received lithium ribbon. Using the die ensured geometric uniformity among samples.

Load data during tensile testing was collected at 100 Hz for nominal strain rates of 5E-1 s^{-1}, 5E-2 s^{-1}, and 5E-3 s^{-1} and at 10 Hz for 5E-4 s^{-1} tests. For the 5E-4 s^{-1} tests, a 5-term Fourier smoothing fit was applied to the data at strains of 0.002 and larger. The strains reported are the nominal (engineering) strains. The displacements measured by the tensile tester were verified to match experimental data during preliminary testing by use of a digital length scale and digital image correlation.

2.4. Finite element analysis

Finite element simulations of the indentation process were conducted to estimate the size of the plastic zones for an analysis of length scale effects on strength. The axisymmetric elastic-plastic simulations (Fig. 3) consisted of rigid indenter with an internal angle of 70.3° (the cone angle which possesses the same self-similar contact area with respect to depth as a Berkovich indenter tip) in contact with a solid mesh of CAX4R elements. Nonlinear geometric effects were included. The elastic behavior of the solid was assumed to be isotropic with an elastic modulus of 9.4 GPa and a Poisson's ratio of 0.3. The behavior of the solid was prescribed as elastic-plastic, with the plastic flow stress defined as a function of plastic strain by inputting stress-strain data from an experimentally measured lithium stress-strain curve collected at 5E-2 s^{-1} strain rate, using a 0.002 strain offset. The "indenter" was specified to have x displacement, z displacement, and all rotations fixed at zero (U1=U3=UR2=UR3=UR1=0) with a displacement downwards by the contact depth (a distance of U2= $-h_c$). The bottom surface of the solid was given a fixed boundary condition, while the left side was given a y-axis symmetric boundary condition. A finite-sliding interaction was defined between the indenter and substrate surface, using surface-to-surface discretization and adjustment only to remove overclosure. This interaction was defined to have frictionless tangential behavior. The simulations produced a plastic volume which, if treated as a hemisphere, has a radius of $11.5^{*}h_c$.

3. Results

The red and black curves in Fig. 4A show the hardness as a function of indenter penetration depth from nanoindentation tests conducted at two different values of $\dot{P}/P$, 0.5 and 0.05 s^{-1}. Each curve is the average of 7 individual tests, with error bars representing one standard deviation. The data is plotted for depths of 0.25 μm (the lower bound for area function calibration) and higher. Plots of the individual indentation load-depth curves, as well as the individual strain rates versus depth, and hardness versus depth can be found in Figs. S7–S10.

Nanoindentation tests are often conducted at constant $\dot{P}/P$ because this condition produces a constant indentation strain rate, $\dot{h}/h$, if the hardness does not vary with depth. However, for the data in Fig. 4A, it is clear that the hardness at smaller depths decreases rapidly before approaching a relatively constant value at larger depths. As a consequence, the depth dependence of the indentation stain rates shown in Fig. 4B also shows a decrease before achieving a relatively constant value. The decrease in hardness at

Fig. 3. The actively yielding elements (AC_Yield output) from ABAQUS used to estimate the volume of the plastic zone under the indenter during nanoindentation experiments. The red elements represent the elements undergoing plastic deformation, while the blue elements undergo elastic deformation only (For interpretation of the references to color in this figure legend, the reader is referred to the web version of this article).

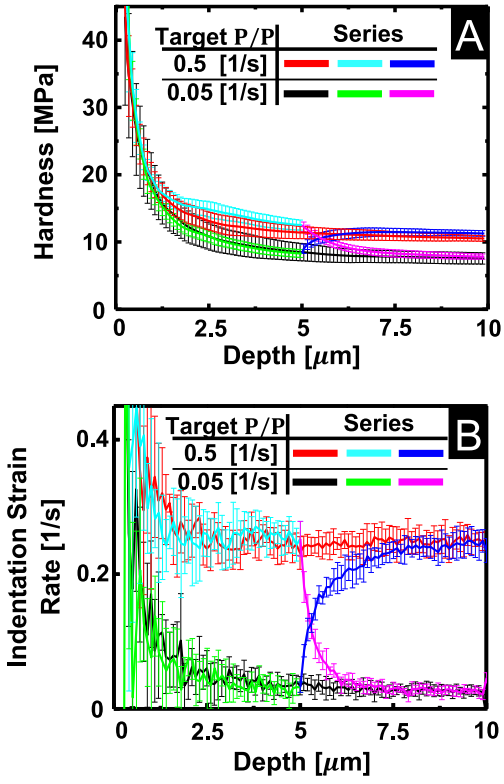

Fig. 4. Nanoindentation tests, with each displayed series representing the average of 7 individual indents conducted under identical test conditions: (A) indentation hardness, and (B) the measured indentation strain rate. Scatter bars span one standard deviation from the mean. The original nanoindentation data and load depth curves can be found in the supporting information.

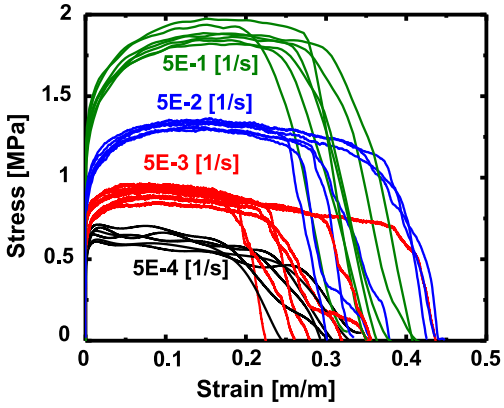

Fig. 5. Stress-strain relationship from uniaxial tension testing of as-received bulk lithium metal, acquired at nominally constant strain rates of 5E-1 [1/s], 5E-2 [1/s], 5E-3 [1/s] and 5E-4 [1/s].

the beginning of the test thus suggests that there is a significant indentation size effect, although some of the decrease may be due to strain rate effects. In addition, we cannot completely rule out the possibility of influences from a hard surface film due to contamination by, for example, oxygen and/or nitrogen. However, if a hard surface film exists, it must be very thin since the elastic modulus data in Fig. 2B show no indication of a different surface layer. Because the hardness appears approximately constant with indentation depth at depths near 10 μm, we fit the hardness and corresponding indentation strain rate to establish the stress exponent for steady state flow ($\frac{\dot{h}}{h} = A * H^n$), which gives a stress exponent of n=6.9. Fig. 4 also includes data from two tests in which $\dot{P}/P$ and the corresponding indentation strain rate was abruptly changed by an order of magnitude at an indentation depth of 5 μm. The curve that transitions from cyan to magenta is for a rate decrease from $\dot{P}/P = 0.5$ s^{-1} to 0.05 s^{-1}, while the curve that changes from green to blue is for a rate increase from $\dot{P}/P = 0.05$ s^{-1} to 0.5 s^{-1}.

The data from these tests indicate that after a brief transient, the hardness and indentation strain rate both recover to the values observed in the tests in which $\dot{P}/P$ was held constant during the entire test, thus indicating a strong strain rate dependence of the hardness, and one that is essentially independent of the loading history. Collectively, the nanoindentation results in Fig. 4 demonstrate that lithium exhibits both size and strain rate dependent hardness (i.e., strength).

Fig. 5 shows results from tensile tests of bulk Li metal. Taking the yield stress as the engineering stress at 0.002 strain, the average yield stresses at strain rates of 5E-1 s^{-1}, 5E-2 s^{-1}, 5E-3 s^{-1} and 5E-4 s^{-1} are 1.26 ± 0.05, 0.89 ± 0.05, 0.71 ± 0.08, and 0.57 ± 0.04 MPa, respectively. Thus, a strong strain rate dependence of the strength is also observed in the tensile tests. Furthermore, the average failure strain does not appear to strongly depend on strain rate and has an average value around 0.35. This is considerably greater than the 0.03 to 0.08 ductilities reported by Tariq et al. [24].

Because the stress-strain curves rise to a near-constant or steady state flow stress, one can use the data obtained in the tensile tests to establish the stress exponent, n, for steady state flow (or creep). To do so, the strain rate dependence of the ultimate stresses (maximum stress measured during the test) in Fig. 5 have been plotted in Fig. 6. The data appear quite linear, suggesting a stress exponent $n = 6.55$, a value in a range that is often indicative of time-dependent plastic deformation controlled by dislocation climb. This value is well within the normal range of approximately 1-7 for most pure metals and alloys [33]. Furthermore, this value appears comparable to the stress exponent as determined for nanoindentation (n=6.9). The stress values determined in this study also match well with recent works of LePage et al. [26] and Masias et al. [25], who note that dislocation climb is likely the

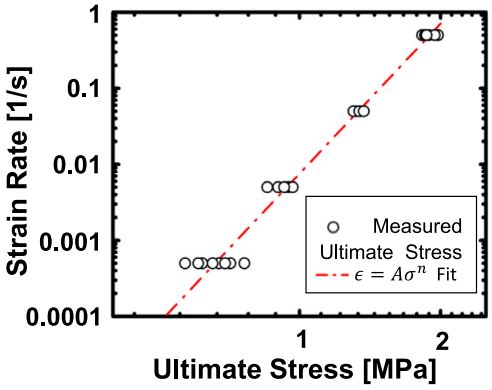

Fig. 6. Strain rate versus ultimate stress from tensile testing results. The trend line represents the curve $\dot{\epsilon} = A\sigma^n$, where A=0.00708 [1/(MPa^n*s)] and n = 6.55.

dominant deformation mechanism for their observed stress exponents of 6.6 and 6.56, respectively.

4. Discussion

4.1. The mechanical properties of Li metal

The data obtained in this study along with that of several previous investigations provides a means by which the strength and plastic flow behavior of lithium can be assessed over a wide range of length and strain rate scales. To do this, data for length scale influences on yield strength from several investigations are plotted in Fig. 7, and data for the strain rate dependencies in Fig. 8. The plots include data from hardness, tension, and compression tests. To facilitate comparison, data from hardness tests have been converted to yield strengths, σ_y, assuming that the Tabor relation is approximately correct, that is, $\sigma_y \cong H/3$. With the aforementioned goal of comparing the tested length scale to a feature size of relevance in the context of a Li metal deposit, we first establish an appropriate length scale for each test. For micropillar and bulk tensile/compression testing, the authors take the square root of the specimen cross sectional area. For indentation testing, the authors use the cube root of the plastic zone size (~11.5*h_c), as determined herein through finite element analysis. The grain size of our specimens (Fig. 1) is 110 ± 20 μm (average ± standard deviation) using the linear intercept technique, based upon the analysis of the area of 350 grains. As such, the plastic zone size is smaller than the grain size at small nanoindentation depths but approaches the grain size at large nanoindentation depths. Data from tension and compression tests are plotted directly as the measured flow strength at 0.1 strain assuming that there is no tension/compression asymmetry, as justified based on the study of Gorgas et al., who found only a minor asymmetry (<10%) between the stress in tension and in compression of Li at room temperature [34]. We note that many of the tests presented in Fig. 7 were performed at different strain rates, thereby potentially conflating effects. However, Fig. 8 shows that the flow stress of Li varies by less than a factor of 10 over strain rates varying by a factor of $>10^6$ from various bulk tests. Thus, the strain rate influences on the data in Fig. 7 are probably less significant than are the size effects.

The strengths measured in this study are plotted in Fig. 7 as a red line [A] for the nanoindentation tests (at $\dot{P}/P$=0.05 [1/s]) and as the red square symbol for the bulk yield strength measured in the tensile tests [B]. The value plotted for yield strength in Fig. 7 (symbol [B]) is the average yield strength measured across the strain rates 5E-4 s^{-1} to 5E-1 s^{-1}, as presented in Fig. 8. The measured H/3 values from nanoindentation decreases precipitously from an initial value near 14 MPa at a representative length scale of ~2.3 μm to nearly 6.7 MPa at a length scale of ~10 μm, and finally 2.5 MPa as the length scale approaches ~115 μm. While the H/3 value from nanoindentation at large depths (2.5 MPa) does not converge to the 0.86 MPa average yield strength measured from bulk testing, some offset between the two quantities may be expected due to factors such as the difference in effective strain rate in the indentation versus the tensile test.

Herbert et al. [21] conducted nanoindentation on lithium thin films deposited using thermal evaporation. For these measurements, denoted [21].1 in Fig. 7 and shown as a dashed blue line, a constant loading rate of 12.5 μN/s was used on an 18 μm thick film, yielding H/3 values that decrease from approximately 60 to 5 MPa as the length scale increases from 0.5 to 10.5 μm. Other nanoindentation results from Herbert et al. were obtained using constant $\dot{P}/P$ experiments on a 5 μm thick film, plotted in Fig. 7 as the solid blue line [21].2. Here, the hardness initially increases until reaching a maximum and subsequently decreases at a length scale of ~4 μm. Herbert et al. argue that this behavior results from a transition from diffusion to dislocation-mediated flow [35]. After the maximum, the data from this study appear to be in fairly good agreement with the results obtained here, that is, displaying similar values of H/3 as the length scale approaches 10 μm.

The micropillar compression results obtained by Xu et al. [22] as plotted as the green line in Fig. 8 also display significant size-dependent strength, with size in the case being the pillar diameter. It should be noted that size-effects may manifest differently in micropillar experiments than in indentation due to differences in the loading and specimen geometry. Furthermore, the lithium used for Xu's study was melted and recrystallized, perhaps possessing significantly larger grains than in as-received lithium. As a result, Xu et al. suggest that their measurements represent single crystal compression, and the corresponding critical resolved shear stress values vary between ~5 and 30 MPa for pillars between 1 μm and 10 μm at a 5E-3 s^{-1} strain rate in their work. Assuming that oxidation exposure and contamination from the gallium focused-ion-beam (or air during transfer) did not affect their results, they observe comparatively higher yield strengths but with generally the same downward trend with length scale observed in this study.

Wang and Cheng [36] combined nanoindentation load-depth curves with an iterative finite element model to report a yield stress of 0.56 MPa under static deformation in as-received lithium metal foil. This data appears on the same order of magnitude as that reported here but slightly lower than others in literature, which may be attributable to a variety of factors such as the uncertainty in indentation strain rate or possible scatter in the data.

A few studies of lithium in bulk polycrystalline form are included in Figs. 7 and 8. Schultz [23] conducted compression testing in atmosphere (air) on 1-11/16" diameter, 1" long cylinders of 98% purity lithium and measured the yield strength in compression as 0.55 MPa at strain rates between 0.08- 0.25 s^{-1}. In a separate study, Tariq et al. [24] measured an average yield stress of 0.85 MPa in tension tests at strain rates between 0.002 – 1.05 s^{-1} using specimens of unspecified size. Their samples exhibited rapid work hardening and failed at or before a strain of 0.08 [m/m]. Masias et al. [25] tested cylindrical specimens of bulk Li in tension and compression, finding a flow stress of 0.74 MPa at a strain rate of 1E-3 s^{-1}. They also observed significantly different behavior between tension and compression, noting that "frictional forces likely played a role in affecting the stress-strain behavior" for their measurements in compression. LePage et al. [26] tested Li foil in tension, finding a flow stress of 0.63 MPa at a strain rate near 3E-4 s^{-1}. Hull and Rosenberg [37] tested bulk samples of Li in tension, finding a yield stress of 0.73 MPa at a strain rate of 1.8E-3 s^{-1}. However, these authors noted the existence of an oxide film on the

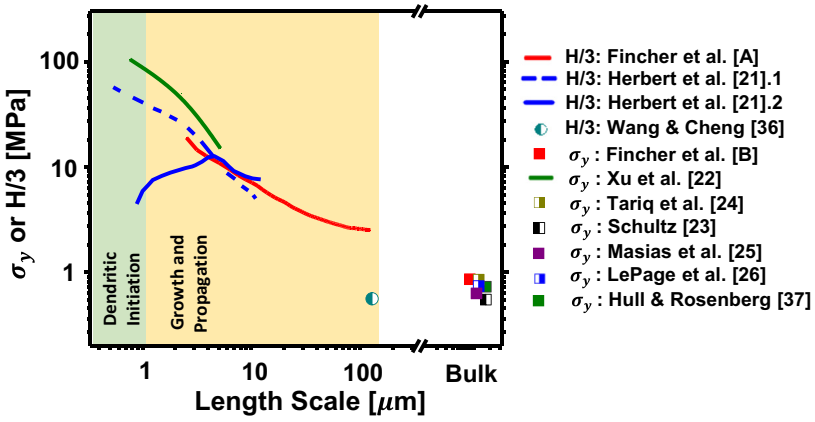

Fig. 7. The σ_y or H/3 is plotted versus a representative length scale, displaying data from this study as well as previous literature. For this study, the yield stress from bulk tensile testing was taken as the flow stress at 10% strain. Feature sizes corresponding to dendritic initiation are shown as a green background, while the yellow region corresponds to dendritic growth and propagation (For interpretation of the references to color in this figure legend, the reader is referred to the web version of this article).

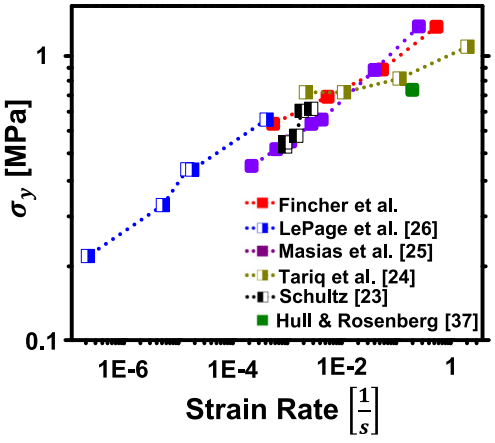

Fig. 8. The yield stress σ_y plotted versus strain rate for bulk tests in this study and in previous literature. (For interpretation of the references to color in this figure legend, the reader is referred to the web version of this article).

specimen, calling into question the role of contamination in their results.

Overall, the bulk testing results in Figs. 7 and 8 seems to indicate that the yield stress of bulk Li metal resides between 0.5 and 1 MPa, depending on the strain rate. Meanwhile, the nanoindentation and pillar compression data indicate that the feature size may play a significant role in Li's response at length scales less than 100 μm.

Going forward, pin-pointing the influence of structure on the mechanical properties of Li metal remains an important task. Of the listed studies in Figs. 7 and 8, only LePage et al. [26] gives the grain size explicitly, with the stated value being 150 μm, similar to the 110 μm measured in this study. While no grain size is stated explicitly in [35], Herbert et al. does show that the grain boundaries can play a significant role in the deformation of Li, based on the applied load required to cause a transition in plastic flow behavior of highly pure Li. However, the grain size and purity of Li metal commonly electrodeposited during battery operation remains unclear.

4.2. Implications for Li metal in battery applications

The size and rate dependency of the yield strength presented in this work likely play a key role in the morphology and reversibility of electrodeposition during electrochemical cycling of Li metal anodes. Analyses have suggested that lithium dendrites initiate with tip radii ranging between 0.1 and 1.5 μm (shown in the green region of Fig. 7) [38–45]. Moreover, electrodeposits have been observed in experiments as having various sizes on the micron scale depending on charging conditions during their formation [10,46–49] (shown in the yellow region of Fig. 7). Likewise, several experiments have already shown an important relationship between the stress applied to electrode stacks by mechanical pressure and the resulting dendrite morphology. In particular, when constrained in a coin-cell geometry, increasing stack pressure has been shown to produce more blunt electrodeposits [11,12]; these flatter electrodeposits benefit from increased uniformity of local current density, leading to increased cycle life [50]. The yield stress (or equivalently, H/3, in hardness testing) represents a maximum stress level of stress that can be imposed on Li electrodeposits prior to permanent deformation (i.e., flattening). As such, the results presented here serve as a basis to estimate the pressure required to blunt electrodeposits of various sizes with the goal of improving performance.

The relevance of deformation mechanics to many other physical processes in lithium metal batteries with liquid electrolytes remains a topic of debate. A recent study by Wang et al. showed that a significant degree of stress accompanies the deposition process itself, even in the absence of an applied stack pressure [51]. Since the chemical potential of a species depends on the applied stress [52,53], the extent to which the local stress modifies the chemical driving forces and plays a role in the homogeneity of electrodeposits warrants further investigation. Beyond reversibility of electrodeposition, so called 'dead Li' remains a significant challenge for the battery community [16,54,55]. Specifically, lithium can detach or fracture from the electrode during cycling, leading to loss of active material and capacity fade. Again, the exact extent to which dead Li formation depends on deformation mechanics is an open topic. Furthermore, while various studies have outlined the relationship between charging rate and dendrite morphology [14,15], more analysis is warranted regarding the extent to which Li's strain-rate dependent strength influences this relationship.

Overall, the results presented herein suggest that work focused on 3D current collectors [56,57], seeding deposition of Li [58], or otherwise tuning the electrodeposit morphology and feature sizes could prove beneficial for achieving stable and reversible Li deposition in liquid electrolyte systems.

Future work should consider focusing on structure-property relationships in lithium, given the influence of microstructure on both its intrinsic underlying mechanics and the electrodeposition process. Indeed, two recent studies of dendritic Li [59] and Mg

[60,61] have shown that dendrites possess significantly different mechanical properties (modulus and hardness) as compared to the bulk material. Whether this alteration occurs due to impurities or from a change in the physical structure of the material (i.e., porosity or crystalline texture) remains an important question. Thus, future studies should seek to understand the influences of impurities, either those present in Li initially or those introduced during cycling, on the mechanical and transport behavior of Li. The grain structure of Li may also play a significant role in the stability of Li metal electrodes. In fact, one previous study has found that grain size of Li can affect the battery's coulombic efficiency [62], while another study showed that a coupling exists between grain texture and electrodeposit morphology [63]. In electroplated systems, grain boundaries increase the local density of activation sites [64]. As a result, the grain boundaries likely act as a "point effect of diffusion," a small disturbance to the local diffusion of ions which could lead to local stress intensifications, as discussed in the recent work of Herbert et al. [65] Additionally, in other metals, grain boundaries have been shown to promote the local formation of passivating films [66]. Thus, ample work remains in understanding the interplay between Li metal's structural evolution and ultimate performance in batteries.

Further chemo-mechanical study also remains in understanding the stability of Li metal deposits. As a BCC metal with a melting temperature of 180.5°C [67], Li's temperature-dependent mechanical properties likely modify the conditions required to maintain a mechanically stable electrode across a range of temperatures. While the work herein studied Li metal at room temperature ($\approx 0.65\ T_m$), the works of LePage et al. [26] as well as of Hull and Rosenberg [37] characterize the temperature dependence of Li's properties across a range of temperatures, where LePage et al. show that the flow stress varies by nearly a factor of three between -75°C and 125°C [26]. Meanwhile, Love et al. [68] show that even the general dendrite morphology changes for different temperatures of practical relevance in a liquid electrolyte system. However, further work studying the coupling of temperature and mechanics in both solid and liquid electrolyte systems would elucidate this important issue further. Additionally, the rate-dependence of plasticity likely plays a key physical role in maintaining stable electrodeposition. While Ferrese and Newman [69] did provide some insight into the effects of plasticity on the stability of Li metal, their work neglected any rate dependency of the plasticity. Jana and Garcia [10] recently showed the effect of rate-dependent plasticity in determining whether a protrusion tends to elongate or flatten under a variety of conditions. However, further chemo-mechanical modelling which incorporates rate-dependent plasticity could provide detailed estimations of the interfacial stresses present in solid-state batteries.

5. Conclusions

Nanoindentation and bulk tensile testing indicate that lithium metal exhibits significant strain rate sensitivity and size dependencies when tested at the nano to bulk-scales. The bulk yield stress of lithium varies from 0.57 to 1.26 MPa for strain rates from 5E-4 s^{-1} to 5E-1 s^{-1}. Tensile tests show that a steady state flow condition is reached at room temperature with a stress exponent of $n = 6.55$, which is comparable to a value of $n = 6.9$ as determined from constant $\dot{P}/P$ nanoindentation tests at 10 μm. The rate-sensitivity of lithium metal suggests that deformation mechanics may play a role in dictating the dendrite morphology, e.g., dendrite morphology depends significantly on current density, i.e., it depends on deposition/strain rate. Nanoindentation tests reveal that the hardness of lithium is not only rate dependent, but that the hardness exhibits significant size effects as well. For indentation tests conducted at constant target $\dot{P}/P = 0.05\ s^{-1}$, the nanoindentation hardness of lithium decreases from about 43 MPa at a depth of 250 nm to about 7.5 MPa (or an equivalent yield stress of 2.8 MPa using a constraint factor of 3) at a depth of 10 μm. Based on finite element analysis, the plastic zone underneath the nanoindentation extends to about 11 times the indentation depth. The length-scale dependency of Li's strength as measured in nanoindentation tests appears to diminish when the contact depth is on the order of tens of microns. Li's size dependent properties may provide a means of tuning the deformation mechanics, and thus perhaps the robustness of the Li anode by adjusting the Li deposit sizes through design of 3D current collectors and seeding the deposition of Li, among other methods. As such, the results presented here may help to guide the design of battery architectures and charging conditions to mitigate unstable growth of Li during electrochemical cycling.

Declaration of Competing Interest

None.

Acknowledgments

C.D.F. acknowledges the support of the National Science Foundation Graduate Research Fellowship under grant No. 1746932. D. O. acknowledges funding through the NSF Research Experiences for Undergraduates program, REU Site Grant (# EEC 1560155). M. P. and Y. Z. acknowledge funding from the mechanical engineering department at Texas A&M University and the Texas A&M Engineering Experimentation Station (TEES). G.M.P.'s contributions to this work were supported in part by the National Science Foundation under grant No. DMR-1743343.

Supplementary materials

Supplementary material associated with this article can be found, in the online version, at doi:10.1016/j.actamat.2019.12.036.

References

[1] N.S. Choi, et al., Challenges facing lithium batteries and electrical double-layer capacitors, Angew. Chem. Int. Ed. 51 (40) (2012) 9994–10024.
[2] L. Porz, et al., Mechanism of lithium metal penetration through inorganic solid electrolytes, Adva. Energy Mater. 7 (20) (2017) 1701003.
[3] H.-K. Tian, Y. Qi, Simulation of the effect of contact area loss in all-solid-state Li-Ion batteries, J. Electrochem. Soc. 164 (11) (2017) E3512–E3521.
[4] R. Koerver, et al., Chemo-mechanical expansion of lithium electrode materials–On the route to mechanically optimized all-solid-state batteries, Energy Environ. Sci. 8 (11) (2018) 2142–2158.
[5] W.J. Li, et al., Fabrication and All Solid-State Battery Performance of TiS_2 /Li10GeP2S12 Composite Electrodes, Mater. Trans. 57 (4) (2016) 549–552.
[6] A.C. Luntz, J. Voss, K. Reuter, Interfacial challenges in solid-state Li ion batteries, J. Phys. Chem. Lett. 6 (22) (2015) 4599–4604.
[7] S. Li, et al., Developing High-Performance Lithium Metal Anode in Liquid Electrolytes, Challenges Progress. Adv Mater 30 (17) (2018) 1706375.
[8] V. Yurkiv, et al., The influence of stress field on Li electrodeposition in Li-metal battery, MRS Commun. 8 (03) (2018) 1285–1291.
[9] C. Monroe, J. Newman, The impact of elastic deformation on deposition kinetics at lithium/polymer interfaces, J. Electrochem. Soc. 152 (2) (2005) A396–A404.
[10] A. Jana, R.E. García, Lithium dendrite growth mechanisms in liquid electrolytes, J. NanoEnergy 41 (2017) 552–565.
[11] L. Gireaud, et al., Lithium metal stripping/plating mechanisms studies, A Metallurg. Appr. 8 (10) (2006) 1639–1649.
[12] D. Wilkinson, et al., Effects of physical constraints on Li cyclability, J. Power Sources 36 (4) (1991) 517–527.
[13] T. Hirai, I. Yoshimatsu, J.i Yamaki, Influence of electrolyte on lithium cycling efficiency with pressurized electrode stack, J. Electrochem. Soc. 141 (3) (1994) 611–614.
[14] M. Dollé, et al., Live scanning electron microscope observations of dendritic growth in lithium/polymer cells, Electrochem. Solid-State Lett. 5 (12) (2002) A286–A289.
[15] C. Brissot, et al., In situ study of dendritic growth inlithium/PEO-salt/lithium cells, J. Electrochem. Acts 43 (10-11) (1998) 1569–1574.

[16] K.N. Wood, M. Noked, N.P. Dasgupta, Lithium Metal Anodes: Toward an Improved Understanding of Coupled Morphological, Electrochemical, and Mechanical Behavior, ACS Energy Lett. 2 (3) (2017) 664–672.
[17] T. Krauskopf, et al., Diffusion limitation of lithium Metal and Li–Mg alloy anodes on LLZO type solid electrolytes as a function of temperature and pressure, Adv. Energy Mater. (2019) 1902568.
[18] J. Sakamoto, More pressure needed, Nature Energy 4 (10) (2019) 827–828.
[19] M.J. Wang, R. Choudhury, J. Sakamoto, Characterizing the Li-Solid-Electrolyte Interface Dynamics as a Function of Stack Pressure and Current Density, Joule 3 (9) (2019) 2165–2178.
[20] Mistry, A. and P. Mukherjee, Molar Volume Mismatch: A Malefactor for Irregular Metallic Electrodeposition in Solid Electrolytes. 2019. doi:10.26434/chemrxiv.10266635.v1.
[21] E.G. Herbert, et al., Nanoindentation of high-purity vapor deposited lithium films: A mechanistic rationalization of diffusion-mediated flow, J. Mater. Res. 33 (10) (2018) 1347–1360.
[22] C. Xu, et al., Enhanced strength and temperature dependence of mechanical properties of Li at small scales and its implications for Li metal anodes, Proc. Natl. Acad. Sci. USA 114 (1) (2017) 57–61.
[23] R.P. Schultz, Lithium: Measurement of Young's Modulus and Yield Strength, Fermi National Accelerator Lab, Batavia, ILUS, 2002.
[24] S. Tariq, et al., Li material testing-fermilab antiproton source lithium collection lens, in: Proceedings of the Particle Accelerator Conference, 2003 *PAC 2003*.
[25] A. Masias, et al., Elastic, plastic, and creep mechanical properties of lithium metal, J. Mater. Sci. 54 (3) (2018) 2585–2600.
[26] W.S. LePage, et al., Lithium Mechanics: Roles of Strain Rate and Temperature and Implications for Lithium Metal Batteries, J. Electrochem. Soc. 166 (2) (2019) A89–A97.
[27] C. Campbell, et al., Effect of nanopatterning on mechanical properties of Lithium anode, Sci. Rep. 8 (1) (2018) 2514.
[28] W.C. Oliver, G.M. Pharr, Measurement of hardness and elastic modulus by instrumented indentation: Advances in understandings and refinements to methodology, J. Mater. Res. 19 (1) (2003) 3–20.
[29] W.C. Oliver, G.M. Pharr, An improved technique for determining hardness and elastic modulus using load and displacement sensing indentation experiments, J. Mater. Res. 7 (6) (1992) 1564–1583.
[30] R.S. Ginder, W.D. Nix, G.M. Pharr, A simple model for indentation creep, J. Mech. Phys. Solids 112 (2018) 552–562.
[31] L.W. Hill, Dynamic mechanical and tensile properties, Paint Coat. Test. Manual 14 (1995) 534.
[32] S. Kalidindi, A. Abusafieh, E. El-Danaf, Accurate characterization of machine compliance for simple compression testing, Exp. Mech. 37 (2) (1997) 210–215.
[33] M.E. Kassner, Fundamentals of Creep in Metals and Alloys, Butterworth-Heinemann, 2015.
[34] I. Gorgas, P. Herke, G. Schoeck, The plastic behaviour of lithium single crystals, Phys. Status Solidi (a) 67 (2) (1981) 617–623.
[35] E.G. Herbert, et al., Nanoindentation of high-purity vapor deposited lithium films: A mechanistic rationalization of the transition from diffusion to dislocation-mediated flow, J. Mater. Res. 33 (10) (2018) 1361–1368.
[36] Y. Wang, Y.-T. Cheng, A nanoindentation study of the viscoplastic behavior of pure lithium, Scr. Mater. 130 (2017) 191–195.
[37] D. Hull, H.M. Rosenberg, The deformation of lithium, sodium, and potassium at low temperatures: tensile and resistivity experiments the philosophical magazine, J. Theoret. Exper. Appl. Phys. 4 (39) (1959) 303–315.
[38] J.W. Gibbs, et al., The Three-Dimensional Morphology of Growing Dendrites, Sci. Rep. 5 (2015) 11824.
[39] A. Jana, D.R. Ely, R.E. García, Dendrite-separator interactions in lithium-based batteries, J. Power Sources 275 (2015) 912–921.
[40] R. Akolkar, Mathematical model of the dendritic growth during lithium electrodeposition, J. Power Sources 232 (2013) 23–28.
[41] J. Barton, J. Bockris, The electrolytic growth of dendrites from ionic solutions, Proc. R. Soc. Lond. A 268 (1335) (1962) 485–505.
[42] J. Diggle, A. Despic, J. Bockris, The mechanism of the dendritic electrocrystallization of zinc, J. Electrochem. Soc. 116 (11) (1969) 1503–1514.
[43] Y. Oren, U. Landau, Growth of zinc dendrites in acidic zinc chloride solutions, Electrochem. Acta 27 (6) (1982) 739–748.
[44] O. Crowther, A.C. West, Effect of electrolyte composition on lithium dendrite growth, J. Electrochem. Soc. 155 (11) (2008) A806–A811.
[45] D.A. Cogswell, Quantitative phase-field modeling of dendritic electrodeposition, Phys. Rev. E 92 (1) (2015) 011301.
[46] C.T. Love, Perspective on the mechanical interaction between lithium dendrites and polymer separators at low temperature, J. Electrochem. Energy Conversi. Storage 13 (3) (2016) 031004.
[47] K. Nishikawa, et al., Li dendrite growth and Li^+ ionic mass transfer phenomenon, J. Electroanal. Chem. 661 (1) (2011) 84–89.
[48] J. Steiger, D. Kramer, R. Mönig, Mechanisms of dendritic growth investigated by in situ light microscopy during electrodeposition and dissolution of lithium, J. Power Sources 261 (2014) 112–119.
[49] J. Steiger, D. Kramer, R. Mönig, Microscopic observations of the formation, growth and shrinkage of lithium moss during electrodeposition and dissolution, Electrochem. Acta 136 (2014) 529–536.
[50] Z. Li, et al., A review of lithium deposition in lithium-ion and lithium metal secondary batteries, J. Power Sources 254 (2014) 168–182.
[51] X. Wang, et al., Stress-driven lithium dendrite growth mechanism and dendrite mitigation by electroplating on soft substrates, Nature Energy 3 (3) (2018) 227.
[52] A.F. Bower, P. Guduru, A simple finite element model of diffusion, finite deformation, plasticity and fracture in lithium ion insertion electrode materials, Model. Simul. Mater. Sci. Eng. 20 (4) (2012) 045004.
[53] R. Xu, K. Zhao, Corrosive fracture of electrodes in Li-ion batteries, J. Mech. Phys. Solids 121 (2018) 258–280.
[54] K.-H. Chen, et al., Dead lithium: mass transport effects on voltage, capacity, and failure of lithium metal anodes, J. Mater. Chem. A 5 (23) (2017) 11671–11681.
[55] I. Yoshimatsu, H. Toshiro, J.-i. Yamaki, Lithium Electrode Morphology during Cycling in Lithium Cells, J. Electrochem. Soc. 135 (10) (1988) 2422–2427.
[56] A. Lahiri, F. Endres, Review—Electrodeposition of Nanostructured Materials from Aqueous, Organic and Ionic Liquid Electrolytes for Li-Ion and Na-Ion Batteries: A Comparative Review, J. Electrochem. Soc. 164 (9) (2017) D597–D612.
[57] X.B. Cheng, et al., Dendrite-Free Lithium Deposition Induced by Uniformly Distributed Lithium Ions for Efficient Lithium Metal Batteries, Adv. Mater 28 (15) (2016) 2888–2895.
[58] X. Guan, et al., Controlling Nucleation in Lithium Metal Anodes, Small 14 (37) (2018) e1801423.
[59] Y. Wang, et al., Mechanical behavior of electroplated mossy lithium at room temperature studied by flat punch indentation, Appl. Phys. Lett. 115 (4) (2019) 043903.
[60] R. Davidson, et al., Formation of magnesium dendrites during electrodeposition, ACS Energy Lett. 4 (2) (2018) 375–376.
[61] R. Davidson, et al., Mapping Mechanisms and Growth Regimes of Magnesium Electrodeposition at High Current Densities, Mater. Horiz. (2019), doi:10.1039/C9MH01367A.
[62] B.L. Mehdi, et al., The impact of Li grain size on coulombic efficiency in Li batteries, Sci. Rep. 6 (2016) 34267.
[63] F. Shi, et al., Strong texturing of lithium metal in batteries, in: Proc. Natl. Acad. Sci., 114, 2017, pp. 12138–12143.
[64] T. Watanabe, Nano-Plating: Microstructure Control theory of Plated Film and Data Base of Plated Film Microstructure, Elsevier, 2004.
[65] E.G. Herbert, et al., On the mechanisms of stress relaxation and intensification at the lithium/solid-state electrolyte interface, J. Mater. Res. 34 (21) (2019) 3593–3616.
[66] L. Wang, et al., Electrochemical corrosion behavior of nanocrystalline Co coatings explained by higher grain boundary density, Electrochim. Acta 52 (13) (2007) 4342–4350.
[67] H. Chandler, Heat Treater's Guide: Practices and Procedures for Nonferrous Alloys, ASM International, 1996.
[68] C.T. Love, O.A. Baturina, K.E. Swider-Lyons, Observation of lithium dendrites at ambient temperature and below, ECS Electrochem. Lett. 4 (2) (2015) A24–A27.
[69] A. Ferrese, J. Newman, Mechanical deformation of a lithium-metal anode due to a very stiff separator, J. Electrochem. Soc. 161 (9) (2014) A1350–A1359.